

# Parametric Dictionary-Based Velocimetry for Echo PIV

Ecaterina Bodnariuc<sup>1</sup>, Stefania Petra<sup>1</sup>, Christian Poelma<sup>2</sup>, and Christoph Schnörr<sup>1</sup>

<sup>1</sup> Image and Pattern Analysis Group, University of Heidelberg, Germany

<sup>2</sup> Laboratory for Aero & Hydrodynamics, Delft University of Technology, The Netherlands

**Abstract.** We introduce a novel motion estimation approach for Echo PIV for the laminar and steady flow model. We mathematically formalize the motion estimation problem as a parametrization of a dictionary of particle trajectories by the physical flow parameter. We iteratively refine this unknown parameter by subsequent sparse approximations. We show smoothness of the adaptive flow dictionary that is a key for a provably convergent numerical scheme. We validate our approach on real data and show accurate velocity estimation when compared to the state-of-the-art cross-correlation method.

## 1 Introduction

Ultrasound techniques are widely used to measure blood flow in clinical applications. They enable noninvasive measurements that can be applied to opaque flows. Echo PIV [8, 11] is a velocimetry technique that applies optical PIV analysis algorithms to sequential ultrasound images and has been developed to improve blood flow analysis using clinical ultrasound machines. Echo PIV involves two steps: an imaging step and a motion estimation step. While the imaging step is rapidly evolving [15, 14, 13], the motion estimation step has been adopted from traditional laser-based imaging [2] and employs cross-correlation techniques prevailing in different fields of experimental fluid dynamics [12, 1]. These techniques have been optimized during the last decade and are widely used by research groups and also as commercial software packages by industry<sup>3</sup>. However, they do not take advantage of *physical motion properties* of the underlying flow in order to effectively regularize flow velocimetry under adverse imaging conditions, as in the case of Echo PIV. Highly accurate motion estimation is of pivotal importance, because subsequent steps of flow analysis, like wall shear stress measurements, rely on *flow derivatives*.

In this paper, we adopt and elaborate a radically different approach [3] for the motion estimation step in Echo PIV. The approach is based on the Poiseuille model for flows in a pipe which yields a one-dimensional parametrization of physically plausible flows. While this model could be refined [16] and even more steps

---

<sup>3</sup> See, e.g. <http://www.lavision.de/en/products/davis.php>

towards the incompressible Navier-Stokes flow model on corresponding bounded domains could be made [7], such additional degrees of freedom quickly turn out to be detrimental for accurate flow estimation under adverse imaging conditions. A second key property exploited by [3] concerns the *sparsity* of microbubbles that are used to seed and to image real flows, as this enables to apply established techniques for sparse estimation and optimization.



**Fig. 1.1.** A schematic representation of the Echo PIV setup (*left*), adapted from [11]. In a rigid cylindrical tube of inner radius  $R = L_z/2$  flows a liquid seeded with microbubbles contrast agents. A linear transducer array is placed along the tube axis, above an observation area of size  $L_x \times L_z$ , and emits a sound pulse into inhomogeneous medium. The same transducer records the back scattered RF (radio frequency) signal. After the signal processing steps, which consists of the Hilbert transform, envelope detection and log-compression, a 2D image is obtained, also known as B-mode image. A sequence of images (*right*) is recorded at a fixed frame rate  $\Delta t^{-1}$ . In the state-of-the-art method, particle image velocimetry (PIV) analysis, the velocity field is estimated by cross-correlating consecutive pairs of B-mode images.

**Contribution.** Our new approach significantly simplifies the approach from [3] and is computationally less expensive. We mathematically formalize the parametrization of a high-dimensional dictionary of particle trajectories by the physical flow parameter. This is exemplified by two corresponding mappings that are continuous and continuously differentiable, respectively. Such properties are key to *provably convergent numerical optimization*, but are missing in [3]. Different established optimization techniques can then be reliably applied, depending on the degree of smoothness of the mapping. Unlike in [3], our approach is validated on *in vitro measurements* of real data, at the limit of standard PIV methods corresponding to low micro-bubble seeding and high flow velocities.

Overall, our approach consistently integrates a basic physical flow model and an adaptively generated trajectory dictionary into a sparse reconstruction framework. This results in a *global spatio-temporal* velocimetry technique that extracts information from the entire given video sequence and therefore is highly accurate and robust. It thus provides a viable alternative to the established (semi-) local cross-correlation techniques.

**Organization.** In Section 2 we give an overview of the proposed method. In Section 3 we describe and characterize in detail the dependency of the flow trajectory matrix on the flow model parameter. Section 4 is devoted to the optimization approach. The method is validated on real data in Section 5. We conclude in Section 6.

## 2 Proposed Approach

In Fig. 1.1 we briefly sketch the basic Echo PIV set-up and refer to [11, 3] for further details.

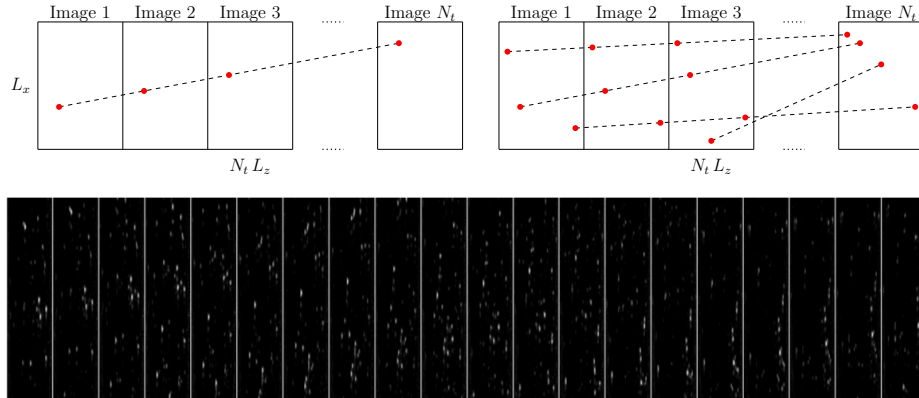


**Fig. 2.1.** Each column in the dictionary  $A(v_m)$  describes a possible trajectory for a single particle seen in  $N_t$  consecutive images concatenated along the tube axis (*top left*, adapted from [3]). The input data  $f$  is given by all  $N_t$  images, which usually contain several particles (*top right*, adapted from [3]). The Poiseuille flow model (3.1) leads to straight line particle trajectories. This can be also observed in the real data example (*bottom*) with  $N_t = 20$  images. The problem is to *sparsely* match particles to trajectories in  $A(v_m^*)$  parametrized by the unknown maximal velocity  $v_m^*$  based on the input data  $f$ .

Let  $f$  denote the input data, which is a sequence of  $N_t$  consecutive images at subsequent time steps merged together as shown in Fig. 2.1. We assume that  $f$  is well-approximated by a sparse superposition of trajectory atoms from a flow dictionary  $A(v_m^*)$ , introduced in Section 3. Hence

$$f \approx A(v_m^*)u(v_m^*), \quad (2.1)$$

where  $u(v_m^*)$  is an indicator vector selecting active trajectories in  $A(v_m^*)$ . If we would know the maximal velocity  $v_m^*$  of the flow profile, then we could trace particles along trajectories by determining the indicator vector  $u(v_m^*)$  via a sparse reconstruction

$$u(v_m^*) = \arg \min_{u \in [0,1]^N} \|A(v_m^*)u - f\|_2^2 + \lambda \|u\|_1, \quad (2.2)$$

provided  $A(v_m^*)$  is nearly an isometry on the class of sparse signals [5]. However  $v_m^*$  is unknown and has to be determined from the input data  $f$ . Our ansatz is to include the estimation of the unknown parameter  $v_m^*$  in the reconstruction step. To this end we denote the non-negative parameter  $v_m$  by  $v \in \mathbb{R}_+$  and we consider the function

$$g(v) = \min_{u \in [0,1]^N} \|A(v)u - f\|_2^2 + \lambda \|u\|_1, \quad (2.3)$$

which will be minimized in order to decrease the “distance” of the input data  $f$  to our unknown parametric linear model  $A(v)u(v)$ . In other words, we are estimating the unknown parameter  $v_m^*$  by adapting a trajectory dictionary to our image sequence. A convergent numerical scheme for minimizing  $g$  is developed in Section 4.

### 3 Flow Dictionary

#### 3.1 Poiseuille flow model

The laminar and steady flow in a straight cylindrical tube of radius  $R$  is governed by the following equations of motion:

$$\begin{cases} x(t) = x(t') + (t - t') v_m \alpha(z) \\ z(t) = z(t') = \text{const.} \end{cases} \quad (3.1)$$

where  $z \in [0, 2R]$ ,  $\alpha(z) = 1 - (R - z)^2/R^2$  and  $t, t' \geq 0$ . The non-negative parameter  $v_m$  is the maximal flow velocity - the velocity of particles moving along the tube axis. Subsequently we will omit index  $m$  and denote  $v_m$  by  $v$ .

#### 3.2 Trajectory Matrix $A(v)$

We further detail the construction of the space-time trajectory dictionary  $A(v)$ , which depends on the maximal flow velocity introduced in (3.1). Let  $\Omega := [0, L_x] \times [0, L_z] \subset \mathbb{R}^2$  denote a fixed field of view in the  $x/z$ -plane, see Fig. 1.1. We uniformly discretize  $\Omega$  into  $N_x N_z$  rectangular cells

$$\Omega_{i,j} := [(i-1)\Delta x, i\Delta x] \times [(j-1)\Delta z, j\Delta z], \quad i \in [N_x], \quad j \in [N_z] \quad (3.2)$$

of size  $\Delta x \Delta z$  with  $\Delta x = L_x/N_x$ ,  $\Delta z = L_z/N_z$ . Using the continuous B-spline basis function of degree one,  $\psi: \mathbb{R} \rightarrow \mathbb{R}$ , or the continuously differentiable B-spline basis function of degree two,  $\varphi: \mathbb{R} \rightarrow \mathbb{R}$ , given by

$$\psi(t) := \begin{cases} 2t, & 0 \leq t < \frac{1}{2}, \\ 2 - 2t, & \frac{1}{2} \leq t \leq 1, \\ 0, & \text{otherwise,} \end{cases} \quad (3.3)$$

$$\varphi(t) := \begin{cases} \frac{9}{2}t^2, & 0 \leq t < \frac{1}{3}, \\ -\frac{3}{2}(1 - 6t + 6t^2), & \frac{1}{3} \leq t < \frac{2}{3}, \\ \frac{9}{2}(1 - 2t + t^2), & \frac{2}{3} \leq t \leq 1, \\ 0, & \text{otherwise,} \end{cases} \quad (3.4)$$

we define for every  $(x_i, z_j) = ((i-1/2)\Delta x, (j-1/2)\Delta z)$  where  $(i, j) \in \{0, \dots, N_x + 1\} \times \{0, \dots, N_z + 1\}$  the cell-centered 2-dimensional basis functions

$$\psi_{i,j}: \mathbb{R}^2 \rightarrow \mathbb{R}, \quad (x, z) \mapsto \psi_{i,j}(x, z) := \psi\left(\frac{x - x_i}{2\Delta x} + \frac{1}{2}\right)\psi\left(\frac{z - z_j}{2\Delta z} + \frac{1}{2}\right), \quad (3.5)$$

$$\varphi_{i,j}: \mathbb{R}^2 \rightarrow \mathbb{R}, \quad (x, z) \mapsto \varphi_{i,j}(x, z) := \varphi\left(\frac{x - x_i}{3\Delta x} + \frac{1}{2}\right)\varphi\left(\frac{z - z_j}{3\Delta z} + \frac{1}{2}\right), \quad (3.6)$$

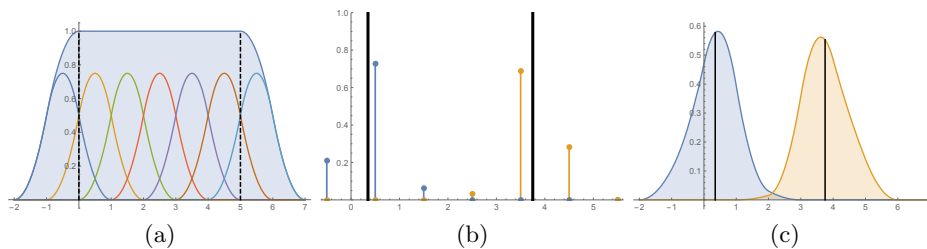


**Fig. 3.1.** (a) Partition of unity of the domain  $[0, 5]$  using the functions (3.4). (b) Two unit-mass Dirac measures located at  $x_1$  and  $x_2$ , respectively, indicated by the two black lines. The corresponding coefficients  $\varphi_i(x_1)$  and  $\varphi_i(x_2)$ , for  $i \in \{0, \dots, 6\}$  are indicated by the blue and yellow points, respectively, located at the cell centroids  $i - 1/2$ . (c) The two functions  $\hat{\delta}_{x_1}(x)$ ,  $\hat{\delta}_{x_2}(x)$  resulting from the basis expansion are used for the representation and matching of real particles. Black lines indicate the centroid position which exactly recover  $x_1$  and  $x_2$ .

which form a partition of unity of  $\Omega$ . Fig. 3.1a illustrates this construction for quadratic function (3.4) in 1D-domain  $[0, L_x]$  with  $L_x = N_x = 5$  and  $\Delta x = 1$ . Note that  $N_x + 2$  basis functions are required and, accordingly,  $(N_x + 2)(N_z + 2)$  basis functions in the 2D case.

The following discussion is developed for the quadratic functions (3.6), and can be easily extended to piecewise linear functions (3.5) by substituting  $\varphi_{i,j}$  with  $\psi_{i,j}$ .

A *point particle* located at  $(x_0, z_0) \in \Omega$  in a 2D-fluid is *mathematically* represent as a Dirac measure  $\delta(x_0, z_0)$  with unit mass. The *discretized representation* is given by the coefficients

$$c_{i,j} = \int_{\mathbb{R}^2} \delta(x_0 - x', z_0 - z') \varphi_{i,j}(x', z') dx' dz' = \varphi_{i,j}(x_0, z_0), \quad (3.7)$$

with  $i \in \{0, \dots, N_x + 1\}$ ,  $j \in \{0, \dots, N_z + 1\}$  and the corresponding function

$$\delta(x_0, z_0) \approx \hat{\delta}_{(x_0, z_0)}(x, z) = \sum_{i=0}^{N_x+1} \sum_{j=0}^{N_z+1} \varphi_{i,j}(x_0, z_0) \varphi_{i,j}(x, z). \quad (3.8)$$

Figs. 3.1b and 3.1c illustrate in the 1D scenario of Fig. 3.1a the coefficients and the functions corresponding to two point particles. Note that the mass of  $\hat{\delta}_{(x_0, z_0)}(x, y)$  is no longer concentrated at  $(x_0, z_0)$  but “smeared over”

$$\text{supp}(\hat{\delta}_{(x_0, z_0)}(x, z)) = \bigcup_{\substack{i-1 \leq i' \leq i+1 \\ j-1 \leq j' \leq j+1}} \Omega_{i', j'} \quad \text{if} \quad (x_0, z_0) \in \Omega_{i, j}, \quad (3.9)$$

that is over the cell containing the location  $(x_0, z_0)$  of the point particle and all adjacent cells. Yet, the representation is still exact in that the point particle can be recovered in terms of its location, which is given by the centroid

$$\begin{pmatrix} x_0 \\ z_0 \end{pmatrix} = \int_{\mathbb{R}^2} \begin{pmatrix} x \\ z \end{pmatrix} \hat{\delta}_{(x_0, z_0)}(x, z) dx dz. \quad (3.10)$$

This larger, but still focused, support of functions representing point particles is a favorable property for matching observed point particles in image sequences of experimental fluids.

Regarding the latter matching task, we set up a dictionary of discretized particle trajectories, based on the flow model (3.1). Specifically, we consider a sequence of  $N_t$  frames imaging the flow within the region  $\Omega$  at time  $t_k = (k-1)\Delta t$ ,  $k \in [N_t]$ . The dictionary is composed of all particle trajectories that meet the center positions  $(x_i, z_j) = ((i-1/2)\Delta x, (j-1/2)\Delta z) \in \Omega_{i,j}$  of all cells given by (3.2). Let us look at a single such trajectory, shown in Fig. 3.2, traced by the particle  $\hat{\delta}_{(x_i, z_j, t_k)}(x, z, t)$  that meets the location  $(x_i, z_j)$  at time point  $t_k$ ,  $k \in [N_t]$ . Due to the flow model (3.1), it moves at each  $t_l$ ,  $l \in [N_t]$  to the space-time points

$$\mathcal{T}_{i,j,k} := \left\{ (x_i + (t_l - t_k)v_m\alpha(z_j), z_j, t_l) : l \in [N_t] \right\}. \quad (3.11)$$

The union of all such sampled trajectories defines the set of space-time positions

$$\mathcal{T} := \bigcup_{i \in [N_x], j \in [N_z], k \in [N_t]} \mathcal{T}_{i,j,k}. \quad (3.12)$$

Let  $x_{il} = x_i + (t_l - t_k)v_m\alpha(z_j)$ , then each space-time position  $(x_{il}, z_j, t_l) \in \mathcal{T}_{i,j,k} \subset \mathcal{T}$  corresponds to a particle  $\delta(x_{il}, z_j, t_l)$ , which for the purpose of numerical matching is approximated by

$$\hat{\delta}_{(x_{il}, z_j, t_l)}(x, z, t) = \sum_{i'=0}^{N_x+1} \sum_{j'=0}^{N_z+1} \varphi_{i',j'}(x_{il}, z_j, t_l) \varphi_{i',j'}(x, z), \quad (3.13)$$

according to (3.8). Note that in the present context of space-time trajectories, it is convenient to index the coefficients  $\varphi_{i',j'}(x_{il}, z_j, t_l)$  also by time, even though only spatial discretization is performed and hence the basis functions (3.6) do not depend on time.

The final step concerns the definition of a matrix  $A$  which collects the coefficients  $\varphi_{i',j'}(x_{il}, z_j, t_l)$  corresponding to all functions (3.13) indexed by  $\mathcal{T}$  of (3.12). We first define the auxiliary function

$$\text{ind}: (i, j, k) \mapsto (k-1)N_x N_z + (j-1)N_x + i, \quad i \in [N_x], j \in [N_z], k \in [N_t] \quad (3.14)$$

which indexes the collection of  $N_t$  cell-discretized domains  $\Omega$  corresponding to the frames of a given image sequence. We now define the matrix

$$A_{\text{ind}(i',j',l), \text{ind}(i,j,k)} := \varphi_{i',j'}(x_{il}, z_j, t_l) \quad (3.15)$$

based on (3.13). In a similar way, we define the matrix  $A$  for piecewise linear functions (3.5), that is,

$$A_{\text{ind}(i',j',l), \text{ind}(i,j,k)} := \psi_{i',j'}(x_{il}, z_j, t_l). \quad (3.16)$$

In words, each column of  $A$  corresponds to the coefficients of the particle approximations (3.13) at locations given by  $\mathcal{T}_{i,j,k}$  of (3.11). We refer to Fig. 3.2 for an illustration.

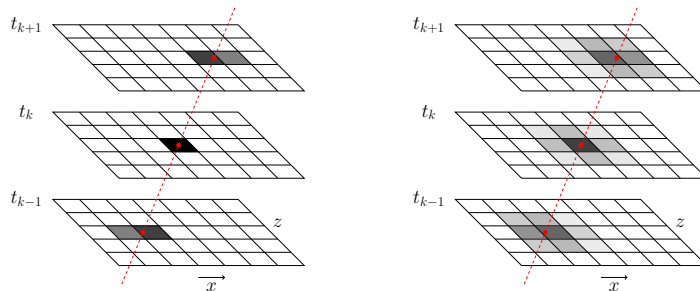


**Fig. 3.2.** Particle trajectory intersecting the region  $\Omega$  at consecutive time steps and the “smeared over” support of functions representing point particles via (left) piecewise linear (3.5) or (right) quadratic (3.6) B-spline basis functions. The figures also illustrate the sparse nature of the matrix  $A(v)$ .

**Lemma 1.** Let  $v \in \mathbb{R}_+$  be a non-negative variable representing the flow parameter  $v_m$  in (3.1). Then (3.15)/(3.16) defines a mapping

$$v \mapsto A(v) \in \mathbb{R}_+^{N \times N}, \quad N = N_x N_z N_t, \quad (3.17)$$

which is continuously differentiable/continuous.

*Proof.* Each entry of  $A$  defined by (3.15)/(3.16) is given by a  $C^1$ -function/  $C$ -function of the form (3.6)/(3.5), which in turn is given by (3.4)/(3.3). By (3.11), the first argument of the right-hand side of (3.15)/(3.16) linearly depends on  $v$ , and so does the first factor of (3.6)/(3.5).

## 4 Optimization

### 4.1 Parametric Optimization

We recast (2.3) as a parametric optimization problem and consider

$$(P_v) \quad \min_{u \in \mathbb{R}^N} J(u, v) \quad \text{s.t.} \quad u \in F(v), \quad (4.1)$$

where  $J(u, v) : \mathbb{R}^N \times \mathbb{R} \rightarrow \mathbb{R}$ ,  $J(u, v) := \|A(v)u - f\|_2^2 + \lambda \|u\|_1$  and  $F(v) := [0, 1]^N$  is the constant feasible set and thus independent of  $v$ . Then  $g$  from (2.3) is the optimal value function of (4.1), given by  $g(v) = \min_{u \in F(v)} J(u, v)$ . We denote by

$S(v) = \arg \min_{u \in F(v)} J(u, v)$  the optimal solution set and investigate continuity of

$v \mapsto g(v)$  and the associated set valued mapping  $v \ni S(v)$ . Continuity of  $g$  is a minimal requirement for reliable numerical optimization. The constraints and the regularization make the minimization of  $J(u, \cdot)$  non-smooth, unless the minimum would be an interior point. But this cannot be expected to hold since constraints will be active and the minimizer will lie on the boundary.

**Theorem 1.** [4, Prop. 4.4] Let  $v_0 \in \mathbb{R}$  be an arbitrary point in the parameter space. Suppose that

- (i) the function  $(u, v) \mapsto J(u, v)$  is continuous on  $\mathbb{R}^N \times \mathbb{R}$ ,
- (ii) the multifunction  $v \rightrightarrows F(v)$  is closed,
- (iii) there exist an  $\alpha \in \mathbb{R}$  and a compact set  $K \subset \mathbb{R}^N$  such that for every  $v$  in a neighborhood of  $v_0$ , the level set

$$\text{lev}_\alpha J(\cdot, v) := \{u \in F(v) : J(u, v) \leq \alpha\} \quad (4.2)$$

- is nonempty and contained in  $K$ ,
- (iv) for any neighborhood  $\mathcal{V}_u$  of the set  $S(v_0)$  there exists a neighborhood  $\mathcal{V}_v$  of  $v_0$  such that  $\mathcal{V}_u \cap F(v) \neq \emptyset$  for all  $v \in \mathcal{V}_v$ .

Then the optimal value function  $g(v)$  is continuous at  $v = v_0$ , and the multifunction  $v \rightrightarrows S(v)$  is upper semi-continuous at  $v_0$ .

**Corollary 1.** *The optimal value function  $g$  from (2.3) is continuous on  $\mathbb{R}$ .*

*Proof.* We apply Thm. 1. (i) holds since  $J$  is continuous in both arguments in view of the definition of  $J$  and the continuity of  $v \mapsto A(v)$  by Lemma 1. (ii), (iv) hold automatically since the feasible set  $F(v) = [0, 1]^N$  is constant and closed. Finally (iii) holds since for any  $v \in \mathbb{R}$  the solution set  $S(v)$  is nonempty in view of the compactness of the feasible set and continuity of  $J(\cdot, v)$ . Hence  $\forall \alpha \geq g(v) \in \mathbb{R}$  we have  $\emptyset \neq S(v) \subset \text{lev}_\alpha J(\cdot, v) \subset [0, 1]^N =: K$ .  $\square$

## 4.2 Optimizing the Value Function

A straightforward way of approximating the minimizer of  $g$  from (2.3) in a range of interest  $a \leq v \leq b$  would be to evaluate the function at a fine grid of points in  $[a, b]$  and choose the one corresponding to the lowest value, compare Fig. 5.1. However, this is a slow and computationally expensive method.

In [9] Mifflin and Strodiot proposed a rapidly converging five-point algorithm closely related to the well-known bisection method [10, Chap. 3] for *continuous* univariate functions, which uses function evaluations, but no derivatives. The method uses function values at five points, denoted and ordered such that

$$\hat{v}_- < v_- < v_0 < v_+ < \hat{v}_+, \quad (4.3)$$

to construct quadratic and polyhedral approximations to the function and then choose a point among the minimizers of the approximating functions via rules that do not require additional function evaluations. This property is significant since every evaluation of  $g$  requires the solution of the  $\ell_1$ -regularized box-constrained least-squares problem (2.2). For further details we refer to the original paper [9]. Results are reported in Section 5.

## 5 Experiments

We applied our method to two challenging in vitro datasets with different flow velocities that follow the Poiseuille flow model assumptions, Sect. 3.1. The first

one corresponds to a slow flow, depicted by very noisy B-mode images, henceforth called data set (a). The second data set (b) corresponds to a very fast flow at the limit of Poiseuille flow assumptions. For each data set we merge  $N_t = 10$  consecutive images (corresponding to the tube interior) to represent the vector  $f$ . In Table 1 we summarize relevant parameters corresponding to both data sets and refer for an illustration to Fig. 1.1.

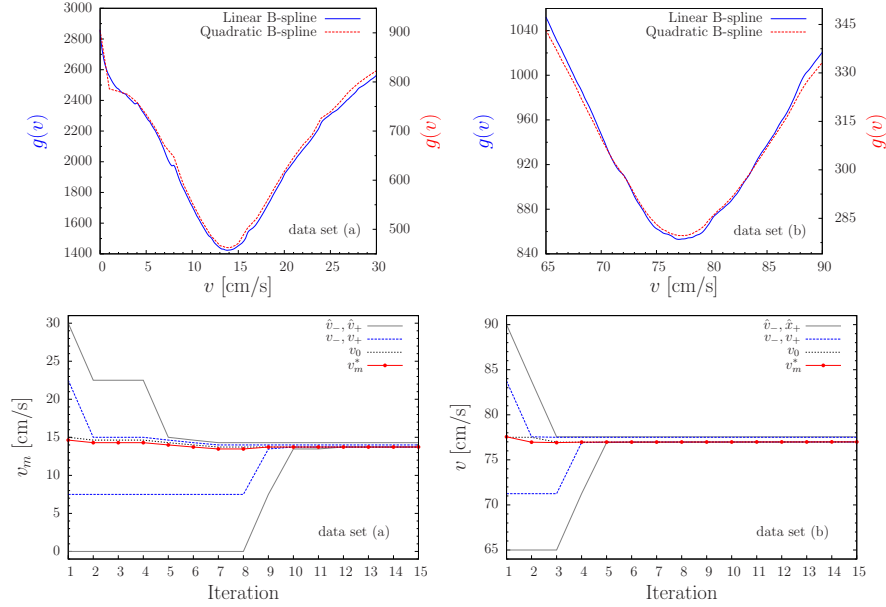


**Fig. 5.1.** Velocity estimation via parametric optimization for data sets (a), l.h.s., and (b), r.h.s. The *top row* plots the parametric function  $g(v)$  defined via the trajectory matrix  $A(v)$  and the corresponding sparse reconstruction. For the data set (a) we set  $\lambda = 0$  and for data set (b) we set  $\lambda = 0.1$ . The coefficients of  $A(v)$  are defined by either piecewise linear (3.16) or quadratic (3.15) B-spline basis functions. The maximal flow velocity  $v_m^*$  is attained at the minimum of  $g(v)$ . The *bottom row* illustrates the performance of the five-point algorithm [9] applied to the two data sets using matrix  $A(v)$  given by (3.16). The five points  $\hat{v}_- < v_- < v_0 < v_+ < \hat{v}_+$  are shown at each iteration step  $k$  with pointed (for  $v_0$ ), dashed (for  $v_-, v_+$ ) and continuous (for  $\hat{v}_-, \hat{v}_+$ ) lines. In both cases they accurately converge to  $v_m^*$ , which is shown in red.

To estimate the maximal velocity  $v_m^*$  we perform univariate minimization of  $v \mapsto g(v)$  as described in Section 4.2. The more involved step is the evaluation of  $g$ . This requires the evaluation of the sparse trajectory matrix  $A(v)$  of size  $N \times N$ ,  $N = N_x N_z N_t$ , but also requires solving the constrained convex optimization problem in (2.3) for certain  $v$  values. These evaluations are performed using CVX [6]. The number of function evaluations is kept low by using the fast converging five-point algorithm [9]. The convergence of this algorithm is illustrated in Fig. 5.1 along with the graph of  $g$ . We refer for results and discussions to Fig. 5.1, Fig. 5.2 and Table 1.

	data set (a)	data set (b)		data set (a)	data set (b)
$L_z = 2R$	0.5 cm	0.5 cm	Cross Correlation, Fig. 5.2	12.76	73.83
$L_x$	4 cm	4 cm	<b>Ours</b> , heuristic, L. B-spline, Fig. 5.1	13.90	77.00
$\Delta t$	1/128 s	1/128 s	<b>Ours</b> , heuristic, Q. B-spline, Fig. 5.1	13.90	77.50
$N_t$	10	10	<b>Ours</b> , exact, L. B-spline, Fig. 5.1	13.73	77.00
$N_x \times N_z$	$64 \times 331$	$64 \times 231$	<b>Ours</b> , exact, Q. B-spline	13.72	77.49

**Table 1.** The columns on the *left* show the data set parameters used in the experiments. The columns on the *right* present the results for maximal velocity  $v_m^*$  (in cm/s) estimated by the proposed approach and compared to the heuristic for minimizing  $g$  on a fine grid (lines 2 & 3) and the cross-correlation results which has been validated against flow meter estimates in previous studies [11].

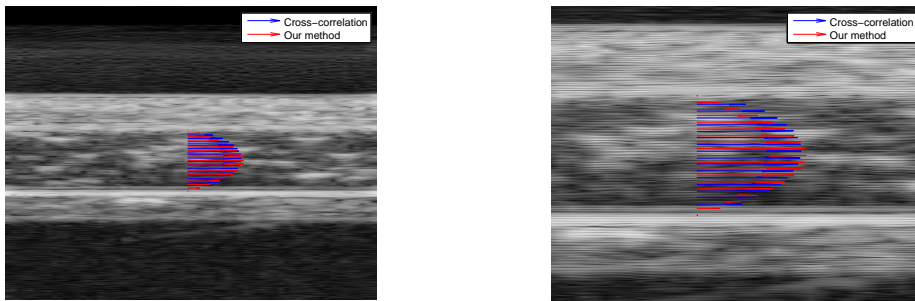


**Fig. 5.2.** Illustration of the velocity field estimated via the cross-correlation method (blue arrows) and our approach (red) for the data set (b). Both methods perform similarly. For numbers we refer to Table 1. The *right* image shows a zoom-in of the result on the left and highlights the poor resolution and noisy nature of B-mode images.

## 6 Conclusion

We have formulated, analyzed and tested on real data the velocity estimation problem in Echo PIV for laminar and steady flows as a parametric sparse reconstruction problem. The sparsifying dictionary consists of space-time trajectories of individual particles, which is adaptively updated during the iterative process and robustly refines the unknown velocity information. We obtain a convergent numerical scheme based on a carefully designed flow dictionary. The comparison with cross-correlation results, demonstrates the robustness of our approach. In addition, our method is completely transparent and not a black-box depending on many fine-tuned parameters. Further work will concentrate on defining the trajectory dictionary using the more general pulsatile blood flow model [16].

**Acknowledgements.** EB, SP and CS thank the German Research Foundation (DFG) for its support via grant GRK 1653.

## References

1. Adrian, R.J. and Westerweel, J.: Particle Image Velocimetry. Cambridge University Press (2011)
2. Adrian, R.J.: Twenty Years of Particle Image Velocimetry. *Experiments in Fluids* 39(2), 159–169 (2005)
3. Bodnariuc, E., Gurung, A., Petra, S., Schnörr, C.: Adaptive Dictionary-Based Spatio-temporal Flow Estimation for Echo PIV. In: Proc. EMMCVPR. LNCS, vol. 8932, pp. 378–391. Springer (2015)
4. Bonnans, J.F., Shapiro, A.: Perturbation Analysis of Optimization Problems. Springer (2000)
5. Foucart, S., Rauhut, H.: A Mathematical Introduction to Compressive Sensing. Birkhäuser Basel (2013)
6. Grant, M., Stephen Boyd, S.: CVX: Matlab Software for Disciplined Convex Programming, version 2.1. <http://cvxr.com/cvx> (Mar 2014)
7. Heywood, J., Rannacher, R., Turek, S.: Artificial Boundaries and Flux and Pressure Conditions for the Incompressible Navier-Stokes Equations. *Int. J. Numer. Meth. Fluids* 22, 325–352 (1996)
8. Kim, H., Hertzberg, J., Shandas, R.: Development and Validation of Echo PIV. *Exp. Fluids* 36(3), 455–462 (2004)
9. Mifflin, R., Strodios, J.J.: A rapidly convergent five-point algorithm for univariate minimization. *Mathematical Programming* 62, 299–319 (1993)
10. Minoux, M.: Mathematical Programming. Theory and Algorithms. John Wiley and Sons (1989)
11. Poelma, C., van der Mijle, R.M.E., Mari, J.M., Tang, M.X., Weinberg, P.D., Westerweel, J.: Ultrasound Imaging Velocimetry: Toward Reliable Wall Shear Stress Measurements. *European Journal of Mechanics - B/Fluids* 35, 70–75 (2012)
12. Raffel, M., Willert, C., Wereley, S., Kompenhans, J.: Particle Image Velocimetry – A Practical Guide. Springer (2007)
13. Rodriguez, S., Deschamps, M., Castaings, M., Ducasse, E.: Guided wave topological imaging of isotropic plates. *Ultrasonics* 54(7), 1880–1890 (2014)
14. Rodriguez, S., Jacob, X., Gibiat, V.: Plane Wave Echo Particle Image Velocimetry. In: Proceedings of Meetings of Acoustics, POMA 19 (2013)
15. Schiffner, M.F., Schmitz, G.: Fast Image Acquisition in Pulse-Echo Ultrasound Imaging using Compressed Sensing. In: Ultrasonics Symposium (IUS), 2012 IEEE International. pp. 1944–1947. IEEE (2012)
16. Womersley, J.: Method for the calculation of velocity, rate of flow and viscous drag in arteries when the pressure gradient is known. *J. Physiol.* 127, 553–563 (1955)